arXiv:1405.1456v1 [astro-ph.HE] 6 May 2014

The Intrinsic Two-Dimensional Size of Sagittarius A*

Geoffrey C. Bower[1,2], Sera Markoff[3], Andreas Brunthaler[4], Casey Law[2], Heino Falcke[5,4,6], Dipankar Maitra[7], M. Clavel[8,9], A. Goldwurm[8,9], M.R. Morris[10], Gunther Witzel[10], Leo Meyer[10], and A.M. Ghez[10]

ABSTRACT

We report the detection of the two-dimensional structure of the radio source associated with the Galactic Center black hole, Sagittarius A*, obtained from Very Long Baseline Array (VLBA) observations at a wavelength of 7mm. The intrinsic source is modeled as an elliptical Gaussian with major axis size $35.4 \times 12.6\, R_S$ in position angle 95 deg East of North. This morphology can be interpreted in the context of both jet and accretion disk models for the radio emission. There is supporting evidence in large angular-scale multi-wavelength observations for both source models for a preferred axis near 95 deg. We also place a maximum peak-to-peak change of 15% in the intrinsic major axis size over five different epochs. Three observations were triggered by detection of near infrared (NIR) flares and one was simultaneous with a large X-ray flare detected by NuSTAR. The absence of simultaneous and quasi-simultaneous flares indicates that not all high energy events produce variability at radio wavelengths. This supports the conclusion that NIR and X-ray flares are primarily due to electron excitation and not to an enhanced accretion rate onto the black hole.

[1]ASIAA, 645 N. A'ohoku Pl., Hilo, HI 96720; gbower@asiaa.sinica.edu.tw

[2]Radio Astronomy Laboratory, UC Berkeley, B-20 Hearst Field Annex, Berkeley, CA 94720-3411

[3]Anton Pannekoek Institute for Astronomy, University of Amsterdam, Science Park 904, 1098XH Amsterdam, The Netherlands

[4]Max-Planck-Institut für Radioastronomie, Auf dem Hügel 69, D-53121 Bonn, Germany

[5]Department of Astrophysics, Institute for Mathematics, Astrophysics and Particle Physics (IMAPP), Radboud University, PO Box 9010, 6500 GL Nijmegen, The Netherlands

[6]ASTRON, P.O. Box 2, 7990 AA Dwingeloo, The Netherlands

[7]Department of Physics and Astronomy, Wheaton College, Norton, MA 02766

[8]AstroParticule et Cosmologie (APC), Université Paris 7 Denis Diderot, 75205 Paris cedex 13, France

[9]Service d'Astrophysique/IRFU/DSM, CEA Saclay, 91191 Gif-sur-Yvette cedex, France

[10]UCLA Division of Astronomy & Astrophysics, Los Angeles, CA, 90095-1562, USA

Subject headings: black hole physics, accretion, galaxies: jets, galaxies: active, Galaxy: center

1. Introduction

The supermassive black hole at the center of our Galaxy, Sagittarius A* (Sgr A*), was first discovered as a bright, compact radio core almost forty years ago (Balick & Brown 1974). In the intervening decades, an enormous and varied body of observational work has focussed on this source, because although Sgr A* shows only weak activity, its proximity offers the chance to observe the accretion flow without confusion from surrounding material (see reviews in, e.g., Melia & Falcke 2001; Genzel et al. 2010; Markoff 2010; Falcke & Markoff 2013).

The radio through submillimeter (submm) spectrum of Sgr A* is inverted, and its polarization, variability and high brightness temperature all indicate an origin in synchrotron emission. The emission has been explained as coming from a jet-like outflow (Falcke & Markoff 2000) or an optically thin accretion flow with particle acceleration (Yuan et al. 2003). Mościbrodzka & Falcke (2013) recently presented a combined jet+inflow model based on GRMHD simulations, that is able to reproduce the intrinsic size and spectrum of Sgr A* well. In that case the major contribution of the size at 7mm wavelength is from the outflow, with the disk providing a smaller contribution. Similar radio properties in nearby low-luminosity active galactic nuclei (LLAGN) have been resolved into weak jets (e.g., M81; Bietenholz et al. 2000) but Very Long Baseline Array (VLBA) observations have revealed no evidence of an elongated core that would be indicative of a jet in Sgr A* (Bower et al. 2006). Larger angular-scale imaging in the Galactic Center, however, has led to several claims for jet-like features (e.g., Yusef-Zadeh et al. 2012; Li et al. 2013). The inverted spectrum requires only that the emission is self-absorbed and stratified, i.e., that increasingly higher frequencies originate in smaller physical scales of the system. Unfortunately, images at lower frequencies, where more pronounced elongation would be expected, are blurred out by an intervening scattering screen (e.g., Bower et al. 2004, 2006; Markoff et al. 2007). Although the scattering effects are weak at short wavelengths, structures at these wavelengths probe regions within ~ 10 Schwarzschild radii ($R_s = 2GM/c^2$) from the black hole (Doeleman et al. 2008), where it is difficult to isolate outflow from inflow. This problem is compounded by the fact that the population of particles emitting synchrotron radiation in quiescence is predominantly quasi-thermal (see, e.g., Markoff 2010) and, thus, provides a smaller photospheric "footprint" compared to the more extended profile that a distribution with a nonthermal power-law component would yield.

Variability provides another tool for probing the structure and physics of Sgr A*. X-ray flares occur daily in Sgr A* with amplitudes from a factor of a few to a factor of > 100; near infrared (NIR) flares appear continuously with on the order of 4 to 6 peaks per day, often appearing simultaneously with X-ray flares (e.g., Yusef-Zadeh et al. 2006a; Nowak et al. 2012). On the other hand, radio and millimeter flux densities vary by much less; at 7 mm variations are $\sim 10\%$ rms on timescales of days (Herrnstein et al. 2004; Macquart & Bower 2006) while at 1.3 mm variations of 100% on timescales of ~ 8 hours are apparent (Dexter et al. 2013). The apparent coupling of NIR and X-ray variability to radio and millimeter variability with an apparent time delay of hours should be treated cautiously given the high frequency of events at all wavelengths and the inability to obtain continuous coverage over 24 hours at radio wavelengths (e.g., Marrone et al. 2008; Eckart et al. 2009; Trap et al. 2011; Eckart et al. 2012; Morris et al. 2012). The overall weak coupling in amplitude between high and low energies suggests that the X-ray and NIR variability may stem from sporadic episodes of particle acceleration in the inner accretion flow or near the base of the jets rather than significant changes in the accretion rate (e.g., Markoff et al. 2001; Yuan et al. 2004; Liu et al. 2004; Dodds-Eden et al. 2011).

The intrinsic size of the radio source is a measure of the photosphere, i.e. the surface at a particular wavelength at which the optical depth is unity. In the jet model, both more efficient particle acceleration and an increased accretion rate, $\dot{M}$, will lead to increased jet photosphere length (Falcke et al. 1993; Markoff et al. 2007). Mościbrodzka et al. (2012) explore accretion disk size scaling with $\dot{M}$ through theory and simulation and find a broader range of scaling relations depending on model details. While the synchrotron cooling time for accelerated particles is < 1000 s for typical conditions near the black hole, any sustained injection or structural changes near the base of the jets, or disruptions ejected as part of an outflow, could lead to variations in the jet photosphere shape that would be detectable through imaging techniques. Depending on the timescales and characteristics of this variability, such as lag (or lead) time compared to the NIR/X-ray flare, VLBA observations during flares can help discern the presence of a jet/outflow, or at the very least better constrain the geometry and emission processes during flares.

In 2012, we participated in the largest ever multi-wavelength campaign focusing on Sgr A* to date, arranged around a 3 Megasecond Chandra HETG "X-ray Visionary Project" [1]. During this campaign we observed 39 new X-ray flares, roughly tripling the number observed and allowing for the first statistical analyses (Nowak et al. 2012; Neilsen et al. 2013). These X-ray flares seem to always be accompanied by simultaneous NIR flaring, though many

[1]XVP; http://www.sgra-star.com

NIR flares are seen without corresponding X-ray activity. The likely explanation is that the quiescent X-ray emission is coming from the outer regions of the accretion flow on much larger scales (Wang et al. 2013), and provides a steady baseline flux that masks smaller nonthermal flares. Unfortunately, it is not possible to generate triggers from Chandra observations on short timescales, but larger NIR flares ($\gtrsim 15 - 20$ mJy) can be considered thresholds of interesting activity near the black hole (Dodds-Eden et al. 2011; Witzel et al. 2012). Thus, we chose to trigger 7mm (43 GHz) VLBA observations based on NIR flares.

The VLBA is able to respond rapidly to external triggers, on timescales as fast as ~ 20 minutes. Both the VLT and the Keck Observatory participated in the campaign, however the relative location of these facilities on the earth compared to the VLBA means that VLT is in a position to generate fast-response triggers for Sgr A*, while from Keck one must wait almost a day for Sgr A* to become visible again, thus probing a much longer timescale. In this paper, we describe the results of both types of triggers (§ 2), compare the observed photosphere to the longterm average based on 10 observations obtained between 1997 and 2002 (§ 3; Bower et al. 2004), and discuss those results in the context of multi-wavelength variability and accretion and outflow theory (§ 4).

2. Methodology, Observations, and Data Reduction

2.1. Methodology

The observed radio image of Sgr A* is an elliptical Gaussian with an axial ratio of $\sim 2:1$ with the major axis in position angle 80 deg East of North. The major axis size scales as λ^2, with a size of ~ 0.7 milliarcseconds at 7 mm, which is strong evidence for the presence of strong interstellar scattering. The intrinsic size as mentioned above is defined by the photosphere at the observing wavelength; the observed size is a convolution of the intrinsic source with the scattering kernel. Sgr A* is heavily resolved by VLBA at this wavelength, making accurate measurement of the size challenging. The orientation of the scattering ellipse is not aligned with the Galactic Plane or other known features. Bower et al. (2014) demonstrate that the scattering likely originates at a distance that is several kpc away from the Galactic Center.

We use closure amplitudes and closure phases to analyze these data (Bower et al. 2004, 2006). The closure amplitude is defined for stations $ijkl$ as

$$C_{ijkl} = \frac{|V_{ij}||V_{kl}|}{|V_{ik}||V_{jl}|}, \tag{1}$$

where V_{ij} is the complex visibility on baseline ij. Two independent permutations are possible

for a set of four stations. The closure phase is the sum of visibility phases on a triangle. The closure amplitude has the property that it is independent of station-based gain factors. This independence removes sensitivity to problems such as elevation- or time-dependent antenna gains due to antenna deformation or changes in atmospheric opacity. In principle, amplitude self-calibration can achieve the same effects but it has limitations in two ways relative to closure amplitude analysis. First, self-calibration can distort the shape of a resolved elliptical Gaussian, especially in a domain of a small number of baselines and of low elevation observations that are strongly affected by phase decorrelation, variable atmospheric opacity, and elevation-dependent pointing and antenna gain factors. Second, error analysis on closure amplitudes effectively takes into account all possible gain solutions, while error analysis of self-calibrated data is only considering one realization of all possible gain solutions. Thus, closure amplitude modeling and error analysis is less precise but more accurate than conventional imaging or visibility analysis of self-calibrated data.

We conducted a test that demonstrates the limits of amplitude self-calibration clearly (Fig. 1). For the data set obtained on 2012 March 19 (described below), we used amplitude self-calibration and visibility modeling to determine sizes. Amplitude self-calibration requires a model, which in this case we took to be a two-dimensional Gaussian with major axis sizes ranging from 450 to 1000 microarcseconds, minor axis sizes equal to 50% of the major axis size, and a position angle of 80 degrees. The self-calibration algorithm (implemented in AIPS task CALIB) was successful in producing a set of calibrated visibilities. The fitted major axis size, however, was strongly dependent on the assumed model: over the range of input sizes, the fitted size ranged from 550 to 900 microarcseconds in a roughly linear trend. For model sizes less than 420 microarcseconds, the source size was best fit as a point source. The median error from the fits was 2.2 microarcseconds, which is significantly smaller than the closure amplitude errors of +14 and −9 microarcseconds. Those self-calibration errors, of course, misrepresent the true errors in the results because they do not incorporate the errors associated with antenna gains. Finally, we note that the self-calibration solution with minimum χ^2 has a major axis size of 724 ± 2 microarcseconds, which is within one σ of the closure amplitude solution, 716^{+14}_{-9} microarcseconds.

An alternative approach is to self-calibrate amplitudes on nearby compact sources. Solutions obtained from this technique are limited by atmospheric and instrumental fluctuations that can give rise to significant errors in amplitudes.

New VLBA observations are significantly more sensitive and accurate than previous VLBA data for Sgr A*, primarily due to the bandwidth upgrade of the VLBA, which increased the recording rate from 256 Mb/s to 2048 Mb/s. The primary effect of this 8× increase in recording rate is the ability to detect Sgr A* at high SNR with shorter integra-

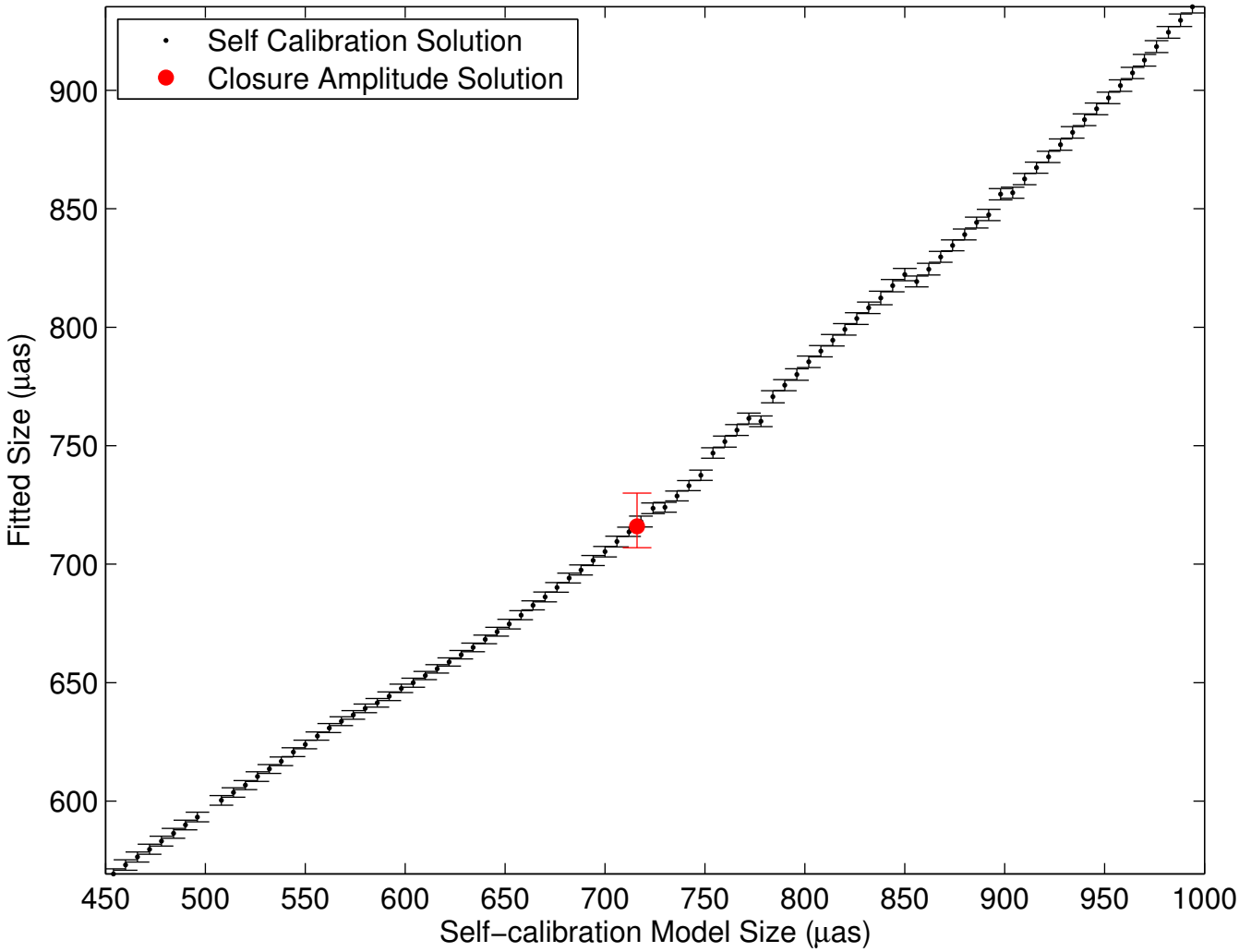

Fig. 1.— A comparison of self-calbration and closure amplitude techniques for the determination of the intrinsic size of a resolved Gaussian source. We compare results for data obtained on 2012 March 19. Self-calibration solutions are plotted as a function of the input self-calibration model. The closure amplitude solution is also plotted, although there is no input model offered. Self-calibration results are heavily dependent on the input model and underestimate true errors. Closure amplitude solutions have a larger error but provide a single answer that is independent of model assumptions and is, therefore, more accurate.

tion times. This permits us to remove the effects of atmospheric decorrelation with shorter fringe-fitting solution intervals, thus eliminating a major source of systematic error in closure amplitude analysis.

2.2. Observations

2.2.1. NIR Observations

In order to select the brightest flares that are most likely to generate power-law electron tails detectable at radio wavelengths, we used a trigger threshold of de-reddened NIR flare flux density of 10 mJy. Dodds-Eden et al. (2011) and Witzel et al. (2012) analyzed the distribution of ≥ 5 years of VLT K_s-band data. They found that flares with a flux density exceeding 10 mJy occur only $\sim 3\%$ of the time and so represent the most luminous end of the flare distribution.

The Sgr A* VLT observation that triggered the VLBA observation on 2012 March 19, was part of the a multi-wavelength campaign that included a 120 ks, 5 half-night, X-ray and NIR campaign performed with XMM-Newton and the VLT in order to study the Sgr A* flaring activity (the detailed results of the campaign will appear in Clavel et al. 2014, in preparation). The NIR data were collected using NACO (NAOS+CONICA), the Laser Guide Star and the filter switching technique already tested in a previous Sgr A* campaign (Trap et al. 2011), for 5 half nights between March 13th and March 21st. These observations were associated with simultaneous observations of Sgr A* in the range 0.1-10 keV with XMM-Newton. On March 19th, using the L' filter (at 3.8 μm) we detected an increase of Sgr A* flux starting around 9:30 UT from an average value of 2 mJy and peaking at about 10 mJy (with preliminary peak value of 11.2 +/- 1.1 mJy) at 10:02 UT, when the alert for VLBA triggering was sent. In the Ks band (at 2.18 μm) the measured peak value was about 5 mJy (preliminary peak value of 5.6 +/- 0.4 mJy). The given IR flux values are de-reddened, using parameters from Fritz et al. (2011). Subsequently, the Sgr A* NIR flux started to decrease until the end of the observation run, five minutes later. During this period, XMM-Newton was pointed at the target while experiencing stable background and low solar activity, but did not detect any X-ray flaring from Sgr A*. The XMM observation ended about 10 minutes after the NIR flare peak and the telescope was not observing during the VLBA observations that started about 20 minutes after the NIR peak.

Both telescopes of the W.M. Keck Observatory were used simultaneously during 4 successive nights: UT 2012 July 20-23 (Witzel 2014). Both used laser guide star adaptive optics corrections. The NIRC2 camera was used on the Keck 2 Telescope with an L' (3.8 μm) filter

and an observing cadence of 20 seconds. The imager on the OSIRIS instrument was used on the Keck 1 Telescope with an H band (1.6 μm) filter and an observing cadence of ~ 50 seconds. Poor weather affected the data acquired on July 21 and 22, but in any case, no major activity was evidenced on those nights. On both July 20 and 23, however, atypically bright flare events were observed. On UT July 20, the flux density of Sgr A* was unusually high throughout the observing period with a peak in the L' band of ~ 18 mJy at 07:15 UT and continued high flux density for two more hours. On July 23, the flux density rose to a high plateau of ~ 10 mJy from a very low value over the time range 07:30 to the end of the observation at 09:30 UT. We adopt fiducial flare times of 08:00 and 08:30 UT for comparison with the VLBA observations on the two successive days, respectively. The flux densities have been dereddened using the L' extinction from Schödel et al. (2010): $A_{L'} = 1.23 \pm 0.08$. Stellar calibrators showed steady flux densities over the observing period.

2.2.2. VLBA Observations

VLBA observations were obtained on five epochs (Table 1). Epochs A, B, and C were obtained following NIR triggers (proposal code BM370), while epochs D and E were scheduled independently of any trigger (proposal code BR173). All epochs included the inner six stations of the VLBA (FD, KP, LA, NL, OV, and PT), with the exception of epoch A in which KP was missing due to snow. The absence of KP significantly reduces sensitivity to the size because it provides many short and intermediate length baselines. Data were obtained at a mean frequency of 43.1 GHz with a recording rate of 2048 Mb/s in both right and left circular polarizations. Initial data processing was performed with AIPS (Greisen 2003). Single band delays were calibrated using observations of bright calibrators including NRAO 530 (J1733-1304) and J1923-2104. Multi-band delays and fringe rates were determined by fringe fitting to Sgr A* itself with a 15-second solution interval. Longer solution intervals introduce phase decorrelation errors. The antenna-based SNR for fringe solutions on a 15-second timescale was > 10. No amplitude calibration was performed on the data. Data were averaged in time to a 30-second time interval and over all frequency channels. Data were exported from AIPS and analyzed with our custom code for closure quantities (Bower et al. 2004).

[p]

We modeled the size of Sgr A* using closure amplitude data derived from the visibilities, as described above. We explored a range of data selection parameters and found that we obtained a minimum in the fitted χ^2_ν for the following parameters: closure amplitude averaging time of 5 minutes; maximum baseline length of 250 Mλ; and minimum antenna

elevation of 10 degrees. Data were analyzed separately in right and left circular polarization correlations. The RCP and LCP results were self-consistent; we averaged the fits together to produce our final results.

The closure amplitude modeling analyzed the data as a resolved elliptical Gaussian with parameters: major axis, b_{maj}, minor axis, b_{min}, position angle, b_{pa}, the total flux density, S, and the noise bias, s. The total flux density is not calibrated but is relative to the noise bias, which corresponds to the rms noise associated with the the 30-second integration time of the visibilities. We assume that the noise bias s is constant for all antennas and all times, which is a simplification that limits the number of free parameters. Representative closure amplitudes are shown in Figure 2. We examined individual closure amplitude values as a function of time to identify bad data points and whether there were periods of significant deviation from the best-fit model. A nonlinear least squares method was used to determine the best-fit parameter values. A grid search of parameters around the best-fit values was used to determine the error surfaces at 1σ and 3σ thresholds. The error surfaces are not normally distributed. We show projections of the error surface in Figure 3 for one experiment and for the average of all experiments. The average of all epochs provides a much stronger constraint on the parameters than a single epoch. We take a conservative approach to determining the errors with two steps: one, we use the projection of the error surface to determine the maximum extent of the acceptable parameter value within a confidence threshold; and, two, we divide the 3σ error estimates by 3 to determine a value for the 1σ error that conveys more information about the bounds of the error distribution. The minor axis, which is nearly aligned North-South, is not as well constrained as the major axis due to the predominantly East-West resolution of the VLBA. In some cases, the 3σ error for the minor axis extends to include a value of zero. Errors for the average are determined by summing together χ^2 surfaces and determining the 3σ surface. Results from modeling are listed in Table 1 along with the mean of all epochs with statistical errors.

We also computed the χ^2_ν for the closure phase under the hypothesis of no axisymmetric structure, for which the closure phase is equal to zero. Individual closure phases determined over an averaging time of 5 minutes had an error of ~ 1 deg with peak-to-peak variations of a few degrees. For data from Epoch B, we calculated $\chi^2_\nu = 1.41$ for $\nu = 654$. We find similar results for the other epochs. Statistically, this is a large deviation from the null hypothesis but it is also explicable as the result of a small underestimate of error in the closure phase or the presence of phase decorrelation. Zero closure phase is consistent with the model of a resolved elliptical Gaussian that we use in this paper. In a future paper, we will explore detailed comparison with non-axisymmetric models of jets and outflows.

We also applied our technique to the calibrator NRAO 530, which was observed in

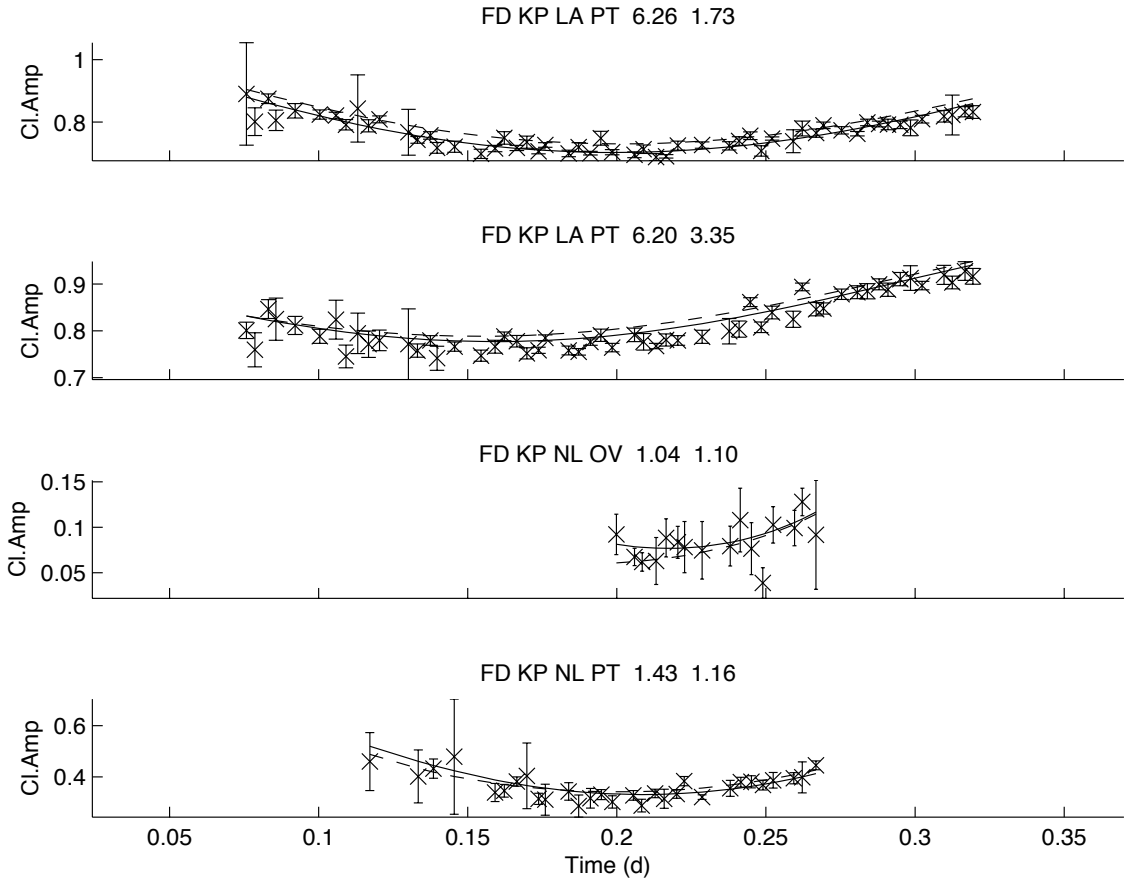

Fig. 2.— A subset of closure amplitudes for data obtained Epoch C in LCP plotted against UT (in fractional days) on the day of observation. For each panel, the stations involved in the closure amplitude quantity are listed along with the χ^2_ν for the average source size and fit source size. The dashed and solid lines show the expected closure amplitudes for the average and fit source sizes, respectively. Results are shown for the two independent closure amplitudes generated from the FD-KP-LA-PT quadrangle. The FD-KP-NL-OV quadrangle shown involves baselines which exceed the maximum baseline length (250 Mλ) for our analysis so that only one quadrangle is included.

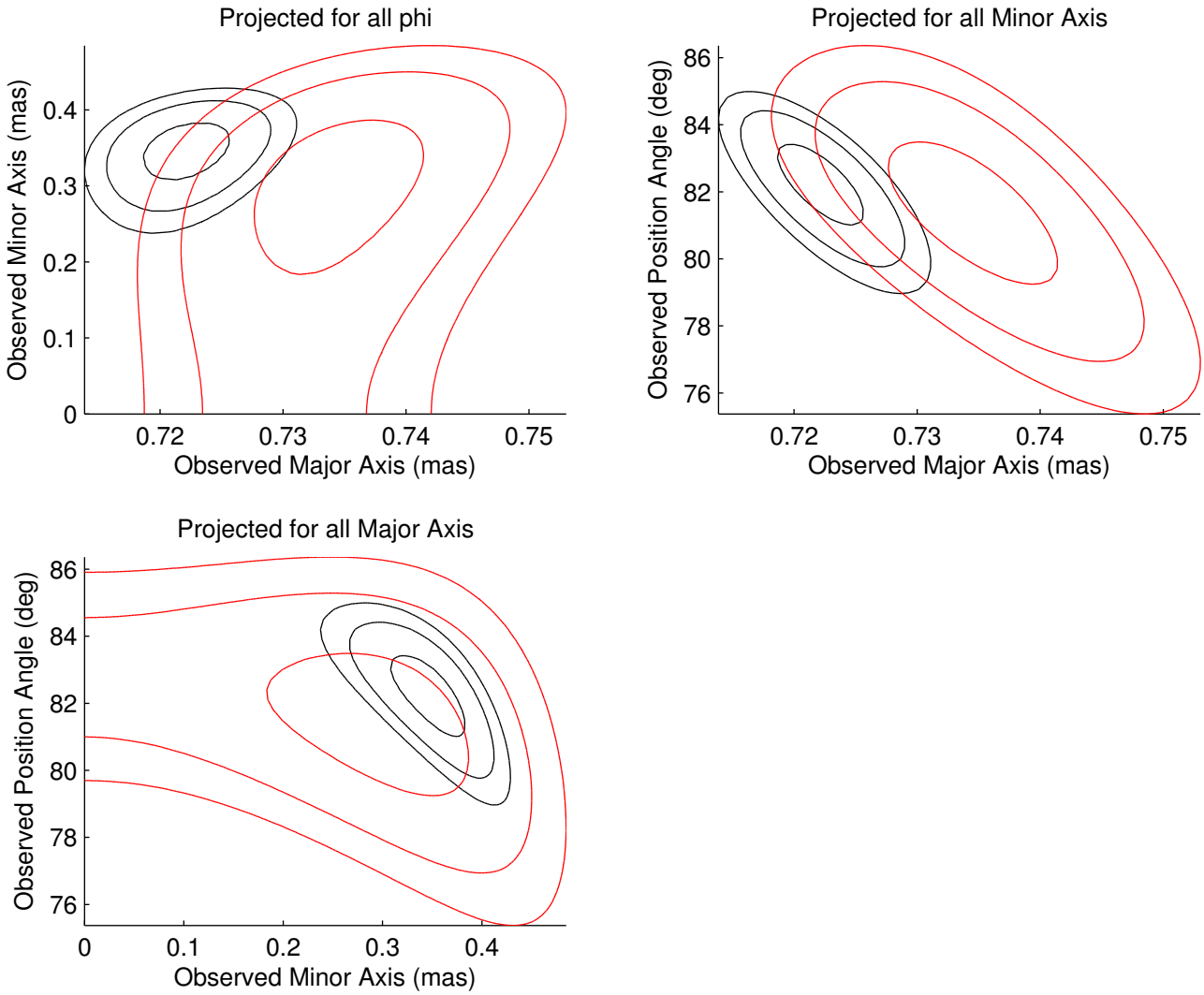

Fig. 3.— Projections of the error surface of the observed size for Epoch C (red contours) and for the average of all epochs (black contours). Panels represent a projection of the three dimensional parameter distribution over all position angles, all minor axis values, and all major axis values. Contours are at 1, 2, and 3 σ thresholds. The figure illustrates the improvement in the accuracy with which we measure the parameters through averaging all of the epochs together.

all epochs. The fitted major and minor axis sizes are shown in Figure 4. Sizes are not determined as accurately for NRAO 530 as for Sgr A*, primarily because of the smaller amount of observing time given to the source. The minor axis size is consistent with no change over time. The major axis clearly changes with time. This can be fit as an apparent velocity of $4.3 \pm 0.4c$. The orientation of the major axis is in position angle -6 ± 3 deg. Past observations have shown that NRAO 530 has exhibited outflows oriented North-South with superluminal velocities of $\sim 7c$ at 3mm (Bower et al. 1997), $2 - 26c$ between 1.3 cm and 3mm (Lu et al. 2011b), and $6 - 27c$ at 2cm (Lister et al. 2013). Our measurements are consistent with this historical evolution. Unfortunately, the evolution of the source size does not permit us to determine an absolute standard for stability of the closure amplitude technique with these data. But we can place some constraints. Excluding the final epoch for which data on NRAO 530 was very limited, the minor axis size shows an rms variation of 5 microarcseconds. This is an order of magnitude less than the typical error of each measurement, suggesting that we are overestimating our errors. The two major axis measurements from 2012 July 21 and 24 differ by only 2 microarcseconds, while errors are $\sim$ 70 microarcseconds. This again suggests that we are overestimating errors in the closure amplitude while achieving substantial accuracy. Future observations would benefit from inclusion of a true point source that does not evolve.

Closure phases for NRAO 530 also exhibited small deviations from zero indicative of asymmetric structure. We measured closure phases that deviated from zero by $\sim \pm 5$ deg. For Epoch B, we calculated $\chi^2_\nu = 6.79$ for $\nu = 109$ in marked contrast to the much smaller values obtained for Sgr A*.

3. The Intrinsic Size

3.1. Two-Dimensional Structure in the Average Size

The intrinsic size is computed by subtracting in quadrature the scattering size from the observed size. Longer wavelength observations determine the scattering size to be an elliptical Gaussian with major axis equal to $(1.31 \pm 0.03)\lambda^2$ milliarcseconds, minor axis equal to $0.64^{+0.05}_{-0.04}\lambda^2$ milliarcseconds, and position angle equal to 78 ± 1 deg, where λ is the wavelength in cm (Bower et al. 2006). Adopting a slightly different major axis scattering scaling constant as we did in Falcke et al. (2009) does not qualitatively alter our conclusions. At the wavelength of these observations, the mean scattering ellipse is 635×310 microarcseconds. The best estimate for the Schwarzschild radius based on observational limits on the black hole mass and distance is 1 $R_S = 10.2 \pm 0.5\mu$as plus systematic errors (Genzel et al. 2010; Falcke & Markoff 2013); we adopt a value of 10 μas for this paper. Intrinsic sizes in the

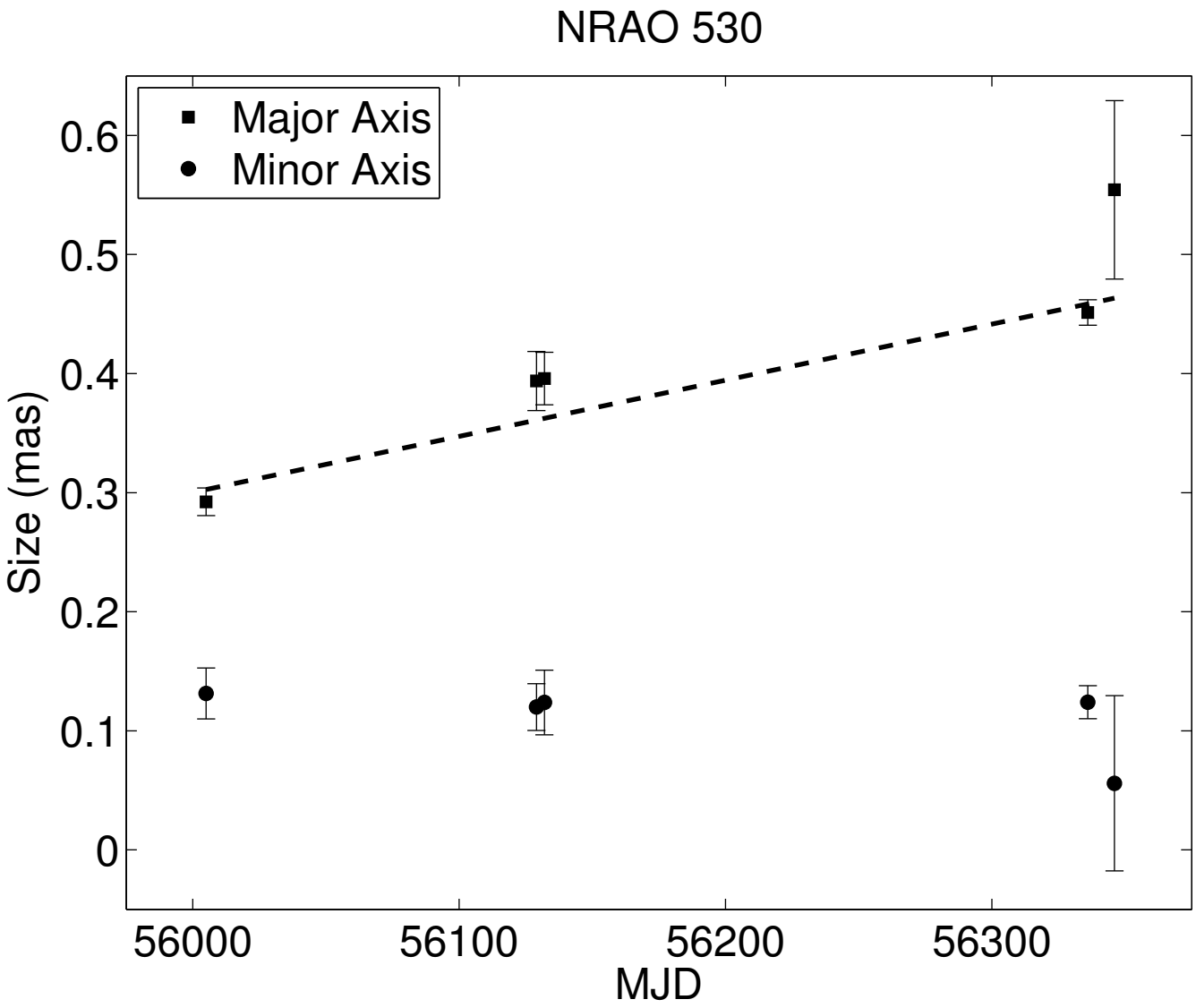

Fig. 4.— Major and minor axis sizes for NRAO 530 as a function of time. The dashed line indicates a fit to the major axis size that corresponds to an apparent velocity of $4.3 \pm 0.4c$.

major axis are presented in Table 1 and plotted as a function of time delay following the peak of the NIR flare or the UT time for non-triggered observations (Fig. 5).

We use the average size from all epochs (Table 1) to determine a two-dimensional intrinsic size for Sgr A*. Deconvolution is performed assuming an intrinsic source and a scattering kernel that are two-dimensional Gaussians. In Figure 6, we show two-dimensional solutions for the intrinsic size for all sizes within the 3σ error surface for which we calculated χ^2 values. The best-fit size is $35.4 \times 12.6\, R_S$ in position angle 95 deg. Errors in the major axis size are $\pm 0.4 R_S$ and in the minor axis size are $+5.5$ and $-4.1\, R_S$. The position angle of the major axis has errors of $+3$ and -4 deg. The observed minor axis size is only $\sim 1\sigma$ larger than the scattering axis, which effectively makes the measurement an upper limit on the intrinsic size. The 3σ upper limit to the intrinsic minor axis size is $29 R_S$. If Sgr A* were circular, then the observed minor axis size would be 460 microarcseconds, which is more than 4σ larger than the measured size. Note that none of the individual epochs show a minor axis size larger than 400 microarcseconds. This demonstrates for the first time at any wavelength that the image of Sgr A* is not circular.

Changing the scattering law alters our results quantitatively but not qualitatively. If we increase the major axis scattering normalization to 1.36 mas cm^{-2}, then the best-fit two-dimensional solution is $31.3^{+0.4}_{-0.4} \times 11.0^{+5.7}_{-3.5} R_S$ in position angle 101^{+7}_{-4} deg. In this case, a circular source size is rejected with a 3σ threshold rather than 4σ.

Past measurements of the intrinsic size have only used the observed major axis size. The mean measured size at the same wavelength from Bower et al. (2004) is 712 ± 11 μas, where the error is based on the scatter in measurements, corresponding to a size $32.4 \pm 2.5 R_S$. If we use the same one-dimensional method to determine the intrinsic size with our new data, we find an average size of $34.4 \pm 0.6 R_S$. Note that the one-dimensional size is slightly smaller than the two-dimensional size. There is no evidence of change in the average one-dimensional intrinsic size of Sgr A* between the Bower et al. (2004) epoch and our new data. This point is striking given the different nature of the two data sets: the older data were not triggered by any measures of activity while the newer data track active states of the system, yet there is no difference in intrinsic size.

3.2. Variability of the Size between Individual Epochs

We find no statistically significant evidence for variability in the observed major axis, minor axis, and position angle among our five epochs. We calculate $\chi^2_\nu = 2.0, 0.8$, and 0.7 with $\nu = 4$ for the three parameters, respectively. While the statistic is larger for the major

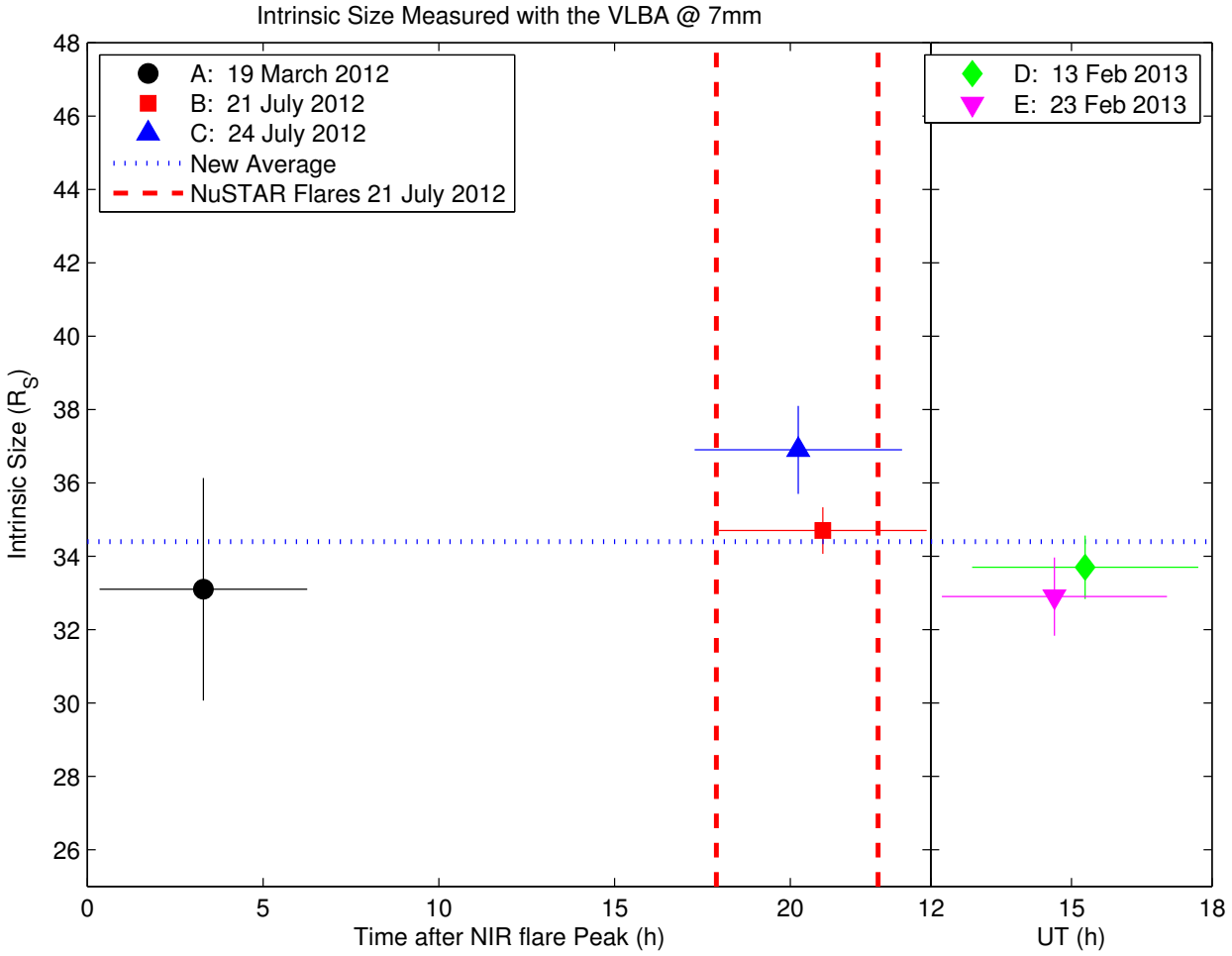

Fig. 5.— One-dimensional intrinsic size as a function of time delay following the peak of the NIR flare for triggered observations (left panel) and as a function of UT for non-triggered observations(right panel). The horizontal error bars indicate the time range over the which the data was obtained. The blue dashed line gives the average size from these observations. Vertical dashed red lines give the time of hard X-ray flares detected by NuSTAR on 21 July 2012 (corresponding to Epoch B).

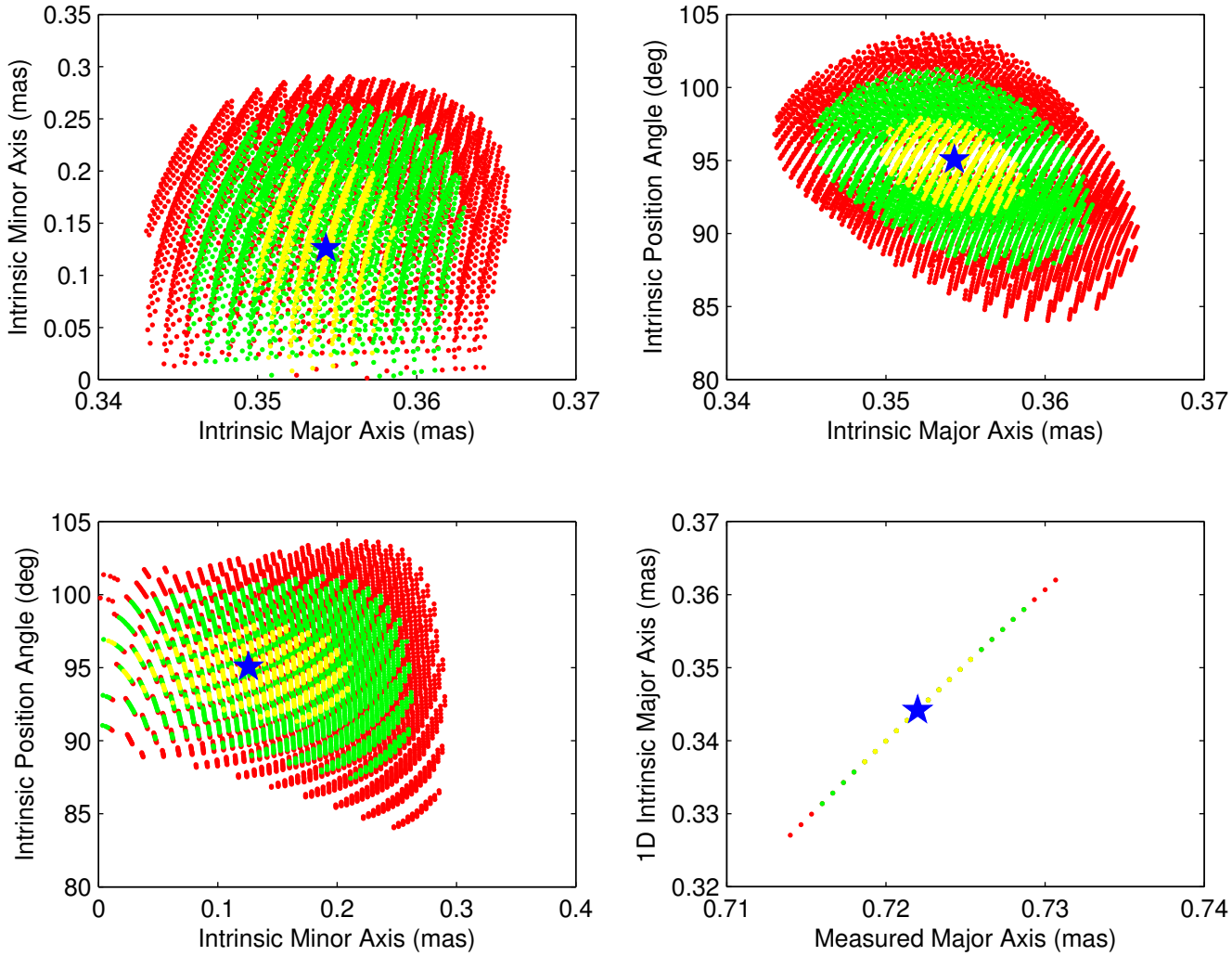
Intrinsic Minor Axis (mas)
Intrinsic Major Axis (mas)
Intrinsic Position Angle (deg)
Intrinsic Major Axis (mas)
Intrinsic Position Angle (deg)
Intrinsic Minor Axis (mas)
1D Intrinsic Major Axis (mas)
Measured Major Axis (mas)

Fig. 6.— Two-dimensional and one-dimensional intrinsic size estimates for Sgr A*. Two-dimensional solutions were obtained through deconvolution of all apparent sizes with the two-dimensional scattering size within the 3σ error surface. Colors show solutions that are $< 1\sigma$ (yellow), between 1 and 2σ (green), and between 2 and 3σ (red). Slices through the parameter space at the position of the best-fit position angle, minor axis, and major axis are shown (upper left, upper right, and lower left, respectively). The blue star indicates the best-fit size. In the lower right panel, we show the intrinsic size that is determined using only the measured major axis size. The same color coding applies to this panel as to the other three panels. The plots show that the maximum intrinsic minor axis value never reaches the minimum permitted value for the major axis; that is, the intrinsic source must be elliptical.

axis, it does not demonstrate significant variability. In Figure 3 we can compare the error surface of Epoch C with that of the average of all epochs. The mean major axis size is offset by only $\sim 2\sigma$.

For individual epochs, we use only the observed major axis size to determine a one-dimensional intrinsic size. The errors on the minor axis from individual epochs are sufficiently large that two-dimensional sizes are not well-constrained. These one-dimensional sizes are listed in Table 1 and Fig. 5. We find an rms variation in the intrinsic size of 5%, with a maximum peak-to-peak change of $\lesssim 15\%$.

We note that the Bower et al. (2004) average size derives from 10 epochs of observation obtained over 5 years. The observations were not triggered and so are likely to represent on average state of Sgr A*. Given the frequency of NIR flares, it is not unlikely that the earlier results represent a comparable level of activity as seen in the new data. One epoch from Bower et al. (2004) did show a formal significant increase in size relative to the mean of $60^{+25}_{-17}\%$ (BB130B; 2001 Jul 29), which was tentatively interpreted as a change in the intrinsic size. The greater sensitivity and reduced systematics of this new experiment makes for a more accurate test of a change in the intrinsic size. We do not see any variability with the amplitude seen in the BB130B epoch, although this does not rule out the possibility that epoch showed actual change in the size.

Akiyama et al. (2013) presents evidence of structural variability in Sgr A* based on VERA observations at 7mm. They report rms variations in the intrinsic size of $\sim 19\%$, which is a factor of several times larger than the rms variability detected here. These results, however, are based on traditional calibration and imaging approaches, which suffer from the systematic problems discussed in § 2. Lu et al. (2011a) also present limits on variability with a maximum amplitude of approximately 20% for 7mm and 3.4 mm observations. Variability in the size of Sgr A* has not been reported at other wavelengths. Long wavelength sizes appear remarkably stable over decades (Bower et al. 2006). Short wavelength sizes have only recently been determined with high precision. Fish et al. (2011) found less than 10% change in the intrinsic size at 1.3mm between observations on consecutive days in which the total intensity changed by $\sim 40\%$.

4. Discussion and Conclusions

The detection of elliptical structure and a preferred axis in the geometry of the emitting region of Sgr A* has important implications. The axial ratio for the intrinsic size is 0.35 with a 3σ upper limit of < 0.85. An elongated structure is a possible signature of a jet but

could also be the result of seeing emission from an elongated accretion flow. The position angle of the elongation is primarily East-West (95^{+3}_{-4} deg). This axis aligns with estimates of jet orientation based on detailed modeling of the Bower et al. (2004) 7mm VLBA data along with spectroscopic constraints, which found a preferred orientation of 105 deg with a large uncertainty (Markoff et al. 2007). The VLBA orientation does not exactly align with any of possible jets that have been recently claimed in the literature through arcsecond-scale imaging. Li et al. (2013), for instance, identify possible jet interaction with the Sgr A West mini-spiral arm and a linear X-ray feature that is directed towards the Southeast of Sgr A* at a position angle of $\sim$ 120 deg. Yusef-Zadeh et al. (2012) associate a series of compact knots and linear features at a position angle of 60 deg. The apparent jet angle could differ between small and large angular scales as is often seen in radio-loud extragalactic sources. If the observed elongation represents an accretion disk, then one might expect a jet to extend North-South. This orientation also does not align with either of the putative jet axes. The East-West orientation also does not align with large scale outflows perpendicular to the Galactic plane (e.g., Sofue & Handa 1984; Su et al. 2010).

On the other hand, X-ray imaging of the quiescent extended emission of Sgr A* has a position angle of 100 deg and axial ratio of $\sim$ 0.5 (Wang et al. 2013). This X-ray elongation is aligned with the disk of young stars orbiting Sgr A* (Yelda et al. 2014). The X-ray emission represents the accretion flow on the scale of the Bondi radius at a scale of $\sim 10^5 R_S$. To interpret the radio source as an accretion flow that is coupled to the outer scale flow requires that the disk orientation remain the same over linear scales that change by four orders of magnitude. In support of this extrapolation, we note that Meyer et al. (2007) do model accretion disk structure on a scale of a few R_S with NIR polarization data and find a χ^2 minimum at position angle 105 deg albeit with large uncertainties. Thus, we find that the VLBA elongation can be viewed as consistent with evidence for both jet and accretion disk hypotheses.

The detection of elliptical structure in our data indicate that shorter wavelength observations that are less obscured by scattering must explore two-dimensional models in order to effectively constrain Schwarzschild-scale structure (Doeleman et al. 2008). Shorter wavelength observations currently do not have sensitivity to elongated structures but that sensitivity will improve as more stations participate in observations. It is uncertain whether the dominant structures at 7mm will be the same as those at 1.3mm, i.e., there could be a transition from a jet-dominated to disk-dominated structures between these wavelengths (e.g., Mościbrodzka & Falcke 2013). The position angle may provide a useful prior to constrain models for short wavelength observations that have very limited coverage of the visibility plane.

We do not find evidence for variations in the size or morphology of the intrinsic size of Sgr A* in these data or in comparison with historical data. The results presented in Fig. 5 show the intrinsic size of Sgr A* for the different experiments. Interestingly, we do not see evidence for a strong "reaction" to NIR, X-ray, or millimeter flares on short (< few hours) timescales. The VLT NIR flare (epoch A) had simultaneous XMM observations that did not detect an X-ray flare. Both of the Keck triggered NIR flares (epochs B and C) were followed by X-ray flares detected by Chandra (Neilsen et al. 2013). The delays between NIR and X-ray flares in these cases are hours, suggesting that they may be unrelated events. For the case of epoch B, the Chandra observation period was not simultaneous with the NIR observations. In the case of epoch C, the Chandra observation period was simultaneous with the NIR observations but do not show a simultaneous detected flare. Epoch B VLBA observations were simultaneous with NuSTAR observations of a very bright flare (Barrière et al. 2014). Millimeter observations with the SMA appeared to show an increase at 1.3mm wavelength from 3.5 to 4.5 Jy between 9 and 10 UT on 23 July, prior to epoch C (D. Marrone, private communication). The NIR flare peaked at 8.5 UT on 23 July. The X-ray flare was detected from 11.8 to 14.0 UT on the same date, beginning after the SMA observations had ended. VLBA observations were obtained approximately 20 hours after these events.

A change in the photosphere size can result primarily from two processes, which may or may not be coupled. In the first case, an increased accretion rate $\dot{M}$ leads to an increased flux but also increases the self-absorption frequency. The exact scaling of the resulting photosphere size with the accretion rate is, thus, very dependent on the details of the source geometry and emission processes. For instance, Falcke et al. (1993) predict the photosphere size to vary $\propto \dot{M}^{2/3}$ for jet models while detailed simulations of accretion disks by Mościbrodzka et al. (2012) give a more complex scaling with $\dot{M}$ for accretion disk systems. If the radio emission is associated with nonthermal particles in the accretion flow, as suggested by Yuan et al. (2003), then an increase in the accretion rate would lead to a size increase in the radio band first, followed by changes in the submm/NIR/X-ray emission. On the other hand if the radio emission is due to an outflow/jet, one would expect the radio photosphere to change only after a rise at NIR and submm wavelengths. Thus, changes in accretion rate would produce variability patterns very dependent on the flow direction, and are thus an important way to deduce the presence of outflows.

On the other hand, changes in the radiating particle distribution will also change the photosphere (see, e.g., Markoff 2010), even if there is no change at all in the accretion rate. For instance an episode of particle acceleration due to magnetic reconnection similar to what is seen in the solar corona would create a power-law component radiating optically thin synchrotron emission (e.g. Markoff et al. 2001; Liu et al. 2004; Dodds-Eden et al. 2009; Trap et al. 2010), and lead to a larger observed size for the duration of the flare. If this

population remains within the inner parts of the accretion flow, it would not likely affect the photosphere at 7mm, which corresponds to larger regions in either the inflow or outflow. However, if the flaring occurs in plasma associated with an outflow, it may be carried with the flow on timescales shorter than the cooling timescales, or reaccelerated, and thus lead to an observable change. A distinguishing characteristic of this model is that these changes would not have to be associated with a change in the actual flux. Unfortunately, the VLBA data do not provide strong constraints on the source flux density. Because the cooling timescale for electrons that create NIR synchrotron emission with conditions near Sgr A* ($B \sim 50 - 100$ G, $n \sim 10^5 - 10^6$ cm^{-3}; Maitra et al. 2009) is less than an hour, the simplest interpretation is that there was a single episode of particle acceleration that cooled before it could affect the 7mm band.

Expanding plasmoid models have also been proposed to characterize the flaring activity of Sgr A* (e.g., Yusef-Zadeh et al. 2006b; Eckart et al. 2006; Yuan et al. 2009). These models attempt to reproduce the spectral evolution of flares with a spherically expanding plasmoid of relativistic electrons. Expansion is typically modeled as sub-relativistic ($v \lesssim 0.01c$) and produces source sizes that are $\sim 1R_S$ at NIR and submm wavelengths. These models have been shown to require complex and possibly *ad hoc* modeling components to fit with actual flares (Trap et al. 2011).

Our results also limit the degree to which refractive scattering effects can alter the size of Sgr A*. The refractive timescale is $t_{ref} \sim \theta D v^{-1}$, where θ is the apparent angular size, D is the distance to the scattering medium from Earth, and v is the relative velocity of the scattering medium to the Earth. Recent observations of the Galactic Center pulsar have shown $D \sim 3$ kpc (Bower et al. 2014). Assuming $v \sim 100$ km s^{-1}, we find $t_{ref} \sim 0.1$ yr at 7 mm. This sets a minimum timescale in which the scattering medium could change entirely. We find no changes to the scattering size on timescales from 2 days to 15 years indicating that the scattering medium is uniform on scales between 10^{12} and 10^{15} cm. Simultaneous shorter wavelength observations could provide an important diagnostic for separating intrinsic from extrinsic changes in the size. The relative stability of the size at 1.3 mm as measured by Fish et al. (2011) where the refractive timescale is ~ 1 day suggest that refractive effects are unimportant but they cannot be ruled out.

We have demonstrated two key results with this work. First, we have measured the two-dimensional size and orientation of the radio source for the first time. This provides special axes for exploring large-scale effects that may be associated with outflows and jets, and accretion flows. A measurement of the frequency-dependent coreshift with phase-referenced VLBI observations is challenging but would confirm the presence and orientation of a jet. Second, we have shown that size variability is very small even in periods of high activity

at NIR and X-ray wavelengths. This absence of source expansion suggests that these NIR and X-ray flares are driven by a single particle acceleration event that does not significantly affect the total energy of the system. Denser multi-wavelength observations are essential to understanding the link between NIR and X-ray variability and the radio source size.

We demonstrate that the closure amplitude technique is the most accurate method for modeling VLBI data on Sgr A*. Our results provide an important proof-of-concept and baseline measurement for future campaigns on Sgr A* during the upcoming G2 encounter. The G2 object is predicted to make a closest approach to Sgr A* in late 2013 or early 2014 and potentially be disrupted and accreted onto the black hole (Gillessen et al. 2012, 2013; Phifer et al. 2013). Further tests of accretion, outflow, and emission models will be obtained with VLBA observations triggered by increases in the millimeter/submillimeter flux density that are driven by increases in the accretion rate.

The National Radio Astronomy Observatory is a facility of the National Science Foundation operated under cooperative agreement by Associated Universities, Inc. We also acknowledge the role of the Lorentz Center, Leiden, and the Netherlands Organization for Scientific Research Vidi Fellowship 639.042.711 for support. S.M. is also grateful for support from The European Community's Seventh Framework Programme (FP7/2007-2013) under grant agreement number ITN 215212 Black Hole Universe. M.C. and A.G. acknowledge the support from the International Space Science Institute to the International Team 216 and the financial support from the UnivEarthS Labex program of Sorbonne Paris Citié (ANR-10-LABX-0023 and ANR-11-IDEX-0005-02). M.C. acknowledges the Université Paris Sud 11 for financial support. Parts of this study is based on observations made with ESO Telescopes at the La Silla Paranal Observatory under the program VM 088.B-1038 and with telescopes on board XMM-Newton, an ESA Science Mission with instruments and contributions directly funded by ESA Member States and the USA (NASA). A.B. was supported by a Marie Curie Outgoing International Fellowship (FP7) of the European Union (project number 275596) H.F. acknowledges funding from an Advanced Grant of the European Research Council under the European Unions Seventh Framework Programme (FP/2007-2013) / ERC Grant Agreement n. 227610. The UCLA Galactic center research group acknowledges supported from NSF grant AST-0909218.

REFERENCES

Akiyama, K., Takahashi, R., Honma, M., Oyama, T., & Kobayashi, H. 2013, PASJ, 65, 91

Balick, B. & Brown, R. L. 1974, ApJ, 194, 265

Barrière, N. M., Tomsick, J. A., Baganoff, F. K., Boggs, S. E., Christensen, F. E., Craig, W. W., Dexter, J., Grefenstette, B., Hailey, C. J., Harrison, F. A., Madsen, K. K., Mori, K., Stern, D., Zhang, W. W., Zhang, S., & Zoglauer, A. 2014, ArXiv e-prints, 1403.0900

Bietenholz, M. F., Bartel, N., & Rupen, M. P. 2000, ApJ, 532, 895

Bower, G. C., Backer, D. C., Wright, M., Forster, J. R., Aller, H. D., & Aller, M. F. 1997, ApJ, 484, 118

Bower, G. C., Deller, A., Demorest, P., Brunthaler, A., Eatough, R., Falcke, H., Kramer, M., Lee, K. J., & Spitler, L. 2014, ApJ, 780, L2

Bower, G. C., Falcke, H., Herrnstein, R. M., Zhao, J., Goss, W. M., & Backer, D. C. 2004, Science, 304, 704

Bower, G. C., Goss, W. M., Falcke, H., Backer, D. C., & Lithwick, Y. 2006, ApJ, 648, L127

Dexter, J., Kelly, B., Bower, G. C., Marrone, D. P., Stone, J., Plambeck, R., & Doeleman, S. S. 2013, MNRAS, submitted

Dodds-Eden, K., Gillessen, S., Fritz, T. K., Eisenhauer, F., Trippe, S., Genzel, R., Ott, T., Bartko, H., Pfuhl, O., Bower, G., Goldwurm, A., Porquet, D., Trap, G., & Yusef-Zadeh, F. 2011, ApJ, 728, 37

Dodds-Eden, K., Porquet, D., Trap, G., Quataert, E., Haubois, X., Gillessen, S., Grosso, N., Pantin, E., Falcke, H., Rouan, D., Genzel, R., Hasinger, G., Goldwurm, A., Yusef-Zadeh, F., Clenet, Y., Trippe, S., Lagage, P.-O., Bartko, H., Eisenhauer, F., Ott, T., Paumard, T., Perrin, G., Yuan, F., Fritz, T. K., & Mascetti, L. 2009, ApJ, 698, 676

Doeleman, S. S., Weintroub, J., Rogers, A. E. E., Plambeck, R., Freund, R., Tilanus, R. P. J., Friberg, P., Ziurys, L. M., Moran, J. M., Corey, B., Young, K. H., Smythe, D. L., Titus, M., Marrone, D. P., Cappallo, R. J., Bock, D., Bower, G. C., Chamberlin, R., Davis, G. R., Krichbaum, T. P., Lamb, J., Maness, H., Niell, A. E., Roy, A., Strittmatter, P., Werthimer, D., Whitney, A. R., & Woody, D. 2008, Nature, 455, 78

Eckart, A., Baganoff, F. K., Morris, M. R., Kunneriath, D., Zamaninasab, M., Witzel, G., Schödel, R., García-Marín, M., Meyer, L., Bower, G. C., Marrone, D., Bautz, M. W., Brandt, W. N., Garmire, G. P., Ricker, G. R., Straubmeier, C., Roberts, D. A., Muzic, K., Mauerhan, J., & Zensus, A. 2009, A&A, 500, 935

Eckart, A., Baganoff, F. K., Schödel, R., Morris, M., Genzel, R., Bower, G. C., Marrone, D., Moran, J. M., Viehmann, T., Bautz, M. W., Brandt, W. N., Garmire, G. P., Ott, T., Trippe, S., Ricker, G. R., Straubmeier, C., Roberts, D. A., Yusef-Zadeh, F., Zhao, J. H., & Rao, R. 2006, A&A, 450, 535

Eckart, A., García-Marín, M., Vogel, S. N., Teuben, P., Morris, M. R., Baganoff, F., Dexter, J., Schödel, R., Witzel, G., Valencia-S., M., Karas, V., Kunneriath, D., Straubmeier, C., Moser, L., Sabha, N., Buchholz, R., Zamaninasab, M., Mužić, K., Moultaka, J., & Zensus, J. A. 2012, A&A, 537, A52

Falcke, H., Mannheim, K., & Biermann, P. L. 1993, A&A, 278, L1

Falcke, H. & Markoff, S. 2000, A&A, 362, 113

Falcke, H., Markoff, S., & Bower, G. C. 2009, A&A, 496, 77

Falcke, H. & Markoff, S. B. 2013, Classical and Quantum Gravity, 30, 244003

Fish, V. L., Doeleman, S. S., Beaudoin, C., Blundell, R., Bolin, D. E., Bower, G. C., Chamberlin, R., Freund, R., Friberg, P., Gurwell, M. A., Honma, M., Inoue, M., Krichbaum, T. P., Lamb, J., Marrone, D. P., Moran, J. M., Oyama, T., Plambeck, R., Primiani, R., Rogers, A. E. E., Smythe, D. L., SooHoo, J., Strittmatter, P., Tilanus, R. P. J., Titus, M., Weintroub, J., Wright, M., Woody, D., Young, K. H., & Ziurys, L. M. 2011, ApJ, 727, L36

Fritz, T. K., Gillessen, S., Dodds-Eden, K., Lutz, D., Genzel, R., Raab, W., Ott, T., Pfuhl, O., Eisenhauer, F., & Yusef-Zadeh, F. 2011, ApJ, 737, 73

Genzel, R., Eisenhauer, F., & Gillessen, S. 2010, Reviews of Modern Physics, 82, 3121

Gillessen, S., Genzel, R., Fritz, T. K., Eisenhauer, F., Pfuhl, O., Ott, T., Schartmann, M., Ballone, A., & Burkert, A. 2013, ApJ, 774, 44

Gillessen, S., Genzel, R., Fritz, T. K., Quataert, E., Alig, C., Burkert, A., Cuadra, J., Eisenhauer, F., Pfuhl, O., Dodds-Eden, K., Gammie, C. F., & Ott, T. 2012, Nature, 481, 51

Greisen, E. W. 2003, in Astrophysics and Space Science Library, Vol. 285, Astrophysics and Space Science Library, ed. A. Heck, 109

Herrnstein, R. M., Zhao, J.-H., Bower, G. C., & Goss, W. M. 2004, AJ, 127, 3399

Li, Z., Morris, M. R., & Baganoff, F. K. 2013, ApJ, 779, 154

Lister, M. L., Aller, M. F., Aller, H. D., Homan, D. C., Kellermann, K. I., Kovalev, Y. Y., Pushkarev, A. B., Richards, J. L., Ros, E., & Savolainen, T. 2013, AJ, 146, 120

Liu, S., Petrosian, V., & Melia, F. 2004, ApJ, 611, L101

Lu, R.-S., Krichbaum, T. P., Eckart, A., König, S., Kunneriath, D., Witzel, G., Witzel, A., & Zensus, J. A. 2011a, A&A, 525, A76

Lu, R.-S., Krichbaum, T. P., & Zensus, J. A. 2011b, MNRAS, 418, 2260

Macquart, J.-P. & Bower, G. C. 2006, ApJ, 641, 302

Maitra, D., Markoff, S., & Falcke, H. 2009, A&A, 508, L13

Markoff, S. 2010, Proceedings of the National Academy of Science, 107, 7196

Markoff, S., Bower, G. C., & Falcke, H. 2007, MNRAS, 379, 1519

Markoff, S., Falcke, H., Yuan, F., & Biermann, P. L. 2001, A&A, 379, L13

Marrone, D. P., Baganoff, F. K., Morris, M. R., Moran, J. M., Ghez, A. M., Hornstein, S. D., Dowell, C. D., Muñoz, D. J., Bautz, M. W., Ricker, G. R., Brandt, W. N., Garmire, G. P., Lu, J. R., Matthews, K., Zhao, J.-H., Rao, R., & Bower, G. C. 2008, ApJ, 682, 373

Melia, F. & Falcke, H. 2001, ARA&A, 39, 309

Meyer, L., Schödel, R., Eckart, A., Duschl, W. J., Karas, V., & Dovčiak, M. 2007, A&A, 473, 707

Morris, M. R., Meyer, L., & Ghez, A. M. 2012, Research in Astronomy and Astrophysics, 12, 995

Mościbrodzka, M. & Falcke, H. 2013, A&A, 559, L3

Mościbrodzka, M., Shiokawa, H., Gammie, C. F., & Dolence, J. C. 2012, ApJ, 752, L1

Neilsen, J., Nowak, M. A., Gammie, C., Dexter, J., Markoff, S., Haggard, D., Nayakshin, S., Wang, Q. D., Grosso, N., Porquet, D., Tomsick, J. A., Degenaar, N., Fragile, P. C., Houck, J. C., Wijnands, R., Miller, J. M., & Baganoff, F. K. 2013, ApJ, 774, 42

Nowak, M. A., Neilsen, J., Markoff, S. B., Baganoff, F. K., Porquet, D., Grosso, N., Levin, Y., Houck, J., Eckart, A., Falcke, H., Ji, L., Miller, J. M., & Wang, Q. D. 2012, ApJ, 759, 95

Phifer, K., Do, T., Meyer, L., Ghez, A. M., Witzel, G., Yelda, S., Boehle, A., Lu, J. R., Morris, M. R., Becklin, E. E., & Matthews, K. 2013, ApJ, 773, L13

Schödel, R., Najarro, F., Muzic, K., & Eckart, A. 2010, A&A, 511, A18

Sofue, Y. & Handa, T. 1984, Nature, 310, 568

Su, M., Slatyer, T. R., & Finkbeiner, D. P. 2010, ApJ, 724, 1044

Trap, G., Goldwurm, A., Dodds-Eden, K., Weiss, A., Terrier, R., Ponti, G., Gillessen, S., Genzel, R., Ferrando, P., Bélanger, G., Clénet, Y., Rouan, D., Predehl, P., Capelli, R., Melia, F., & Yusef-Zadeh, F. 2011, A&A, 528, A140

Trap, G., Goldwurm, A., Terrier, R., Dodds-Eden, K., Gillessen, S., Genzel, R., Pantin, E., Lagage, P. O., Ferrando, P., Bélanger, G., Porquet, D., Grosso, N., Yusef-Zadeh, F., & Melia, F. 2010, Advances in Space Research, 45, 507

Wang, Q. D., Nowak, M. A., Markoff, S. B., Baganoff, F. K., Nayakshin, S., Yuan, F., Cuadra, J., Davis, J., Dexter, J., Fabian, A. C., Grosso, N., Haggard, D., Houck, J., Ji, L., Li, Z., Neilsen, J., Porquet, D., Ripple, F., & Shcherbakov, R. V. 2013, Science, 341, 981

Witzel, G. 2014, in American Astronomical Society Meeting Abstracts, Vol. 223, American Astronomical Society Meeting Abstracts, #238.04

Witzel, G., Eckart, A., Bremer, M., Zamaninasab, M., Shahzamanian, B., Valencia-S., M., Schödel, R., Karas, V., Lenzen, R., Marchili, N., Sabha, N., Garcia-Marin, M., Buchholz, R. M., Kunneriath, D., & Straubmeier, C. 2012, ApJS, 203, 18

Yelda, S., Ghez, A. M., Lu, J. R., Do, T., Meyer, L., Morris, M. R., & Matthews, K. 2014, ApJ, 783, 131

Yuan, F., Lin, J., Wu, K., & Ho, L. C. 2009, MNRAS, 395, 2183

Yuan, F., Quataert, E., & Narayan, R. 2003, ApJ, 598, 301

—. 2004, ApJ, 606, 894

Yusef-Zadeh, F., Arendt, R., Bushouse, H., Cotton, W., Haggard, D., Pound, M. W., Roberts, D. A., Royster, M., & Wardle, M. 2012, ApJ, 758, L11

Yusef-Zadeh, F., Bushouse, H., Dowell, C. D., Wardle, M., Roberts, D., Heinke, C., Bower, G. C., Vila-Vilaró, B., Shapiro, S., Goldwurm, A., & Bélanger, G. 2006a, ApJ, 644, 198

Yusef-Zadeh, F., Roberts, D., Wardle, M., Heinke, C. O., & Bower, G. C. 2006b, ApJ, 650, 189

This preprint was prepared with the AAS LaTeX macros v5.2.

Table 1. Size of Sgr A*

Epoch	Date	UT Start (days)	UT End (days)	b_{maj} (μas)	b_{min} (μas)	b_{pa} (deg)	σ_{int} (R_S)
A	19 March 2012	0.431	0.677	716^{+16}_{-11}	400^{+53}_{-133}	$83.3^{+3.7}_{-4.6}$	$33.1^{+3.0}_{-2.7}$
B	21 July 2012	0.082	0.328	723^{+3}_{-3}	315^{+37}_{-70}	$83.0^{+1.0}_{-1.2}$	$34.7^{+0.6}_{-0.7}$
C	24 July 2012	0.074	0.320	734^{+6}_{-5}	300^{+61}_{-100}	$81.5^{+1.6}_{-2.0}$	$36.9^{+1.2}_{-1.1}$
D	13 Feb 2013	0.537	0.738	719^{+4}_{-4}	390^{+27}_{-36}	$81.2^{+1.2}_{-1.6}$	$33.7^{+0.9}_{-0.8}$
E	23 Feb 2013	0.510	0.710	715^{+5}_{-4}	392^{+52}_{-131}	$79.1^{+2.0}_{-3.3}$	$32.9^{+1.1}_{-0.9}$
AVG	...	...	...	722^{+3}_{-3}	345^{+28}_{-35}	$82.4^{+0.8}_{-1.1}$	$34.4^{+0.6}_{-0.6}$